Investigation of the stability of graphene devices for quantum resistance metrology at direct and alternating current

OPEN ACCESS
IOP Publishing
Measurement Science and Technology
Meas. Sci. Technol. **33** (2022) 065012 (11pp)
https://doi.org/10.1088/1361-6501/ac4a1a

Investigation of the stability of graphene devices for quantum resistance metrology at direct and alternating current

Dong-Hun Chae[1,*], Mattias Kruskopf[2,*], Jan Kucera[3,*], Jaesung Park[1], Ngoc Thanh Mai Tran[4,5], Dan Bee Kim[1], Klaus Pierz[2], Martin Götz[2], Yefei Yin[2], Pavel Svoboda[3], Petr Chrobok[3], François Couëdo[6] and Félicien Schopfer[6]

[1] Korea Research Institute of Standards and Science (KRISS), Daejeon 34113, Republic of Korea
[2] Physikalisch-Technische Bundesanstalt (PTB), Bundesallee 100, 38116 Braunschweig, Germany
[3] Czech Metrology Institute (CMI), Okružní 31, 638 00 Brno, Czech Republic
[4] Istituto Nazionale di Ricerca Metrologica (INRIM), Strada delle Cacce, 91, 10135 Torino, Italy
[5] Politecnico di Torino, Corso Duca degli Abruzzi 24, 10129 Torino, Italy
[6] Laboratoire National de Métrologie et d'Essais (LNE), 29 Avenue Roger Hennequin, 78197 Trappes, France

E-mail: dhchae@kriss.re.kr, Mattias.Kruskopf@ptb.de and jkucera@cmi.cz

Received 27 October 2021, revised 23 December 2021
Accepted for publication 11 January 2022
Published 9 March 2022

Abstract

Interlaboratory comparisons of the quantized Hall resistance (QHR) are essential to verify the international coherence of primary impedance standards. Here, we report on the investigation of the stability of p-doped graphene-based QHR devices at direct and alternating currents at CMI, KRISS, and PTB. To improve the stability of the electronic transport properties of the polymer-encapsulated devices, they were shipped in an over-pressurized transport chamber. The agreement of the quantized resistance with $R_K/2$ at direct current was on the order of 1 nΩ Ω^{-1} between 3.5 and 7.5 T at a temperature of 4.2 K despite changes in the carrier density during the shipping of the devices. At alternating current, the quantized resistance was realized in a double-shielded graphene Hall device. Preliminary measurements with digital impedance bridges demonstrate the good reproducibility of the quantized resistance near the frequency of 1 kHz within 0.1 $\mu\Omega$ Ω^{-1} throughout the international delivery.

Supplementary material for this article is available online

Keywords: quantum Hall effect, quantized Hall resistance, graphene, impedance standard, F4-TCNQ doping, stability

(Some figures may appear in colour only in the online journal)

* Authors to whom any correspondence should be addressed.

1. Introduction

Soon after the first realization of monolayer graphene, it was demonstrated that the unique band structure of this two-dimensional hexagonal carbon lattice enables robust Hall resistance quantization even at room temperature [1]. This has initiated many studies in electrical quantum metrology intending to realize resistance standards that can be used at higher temperatures and lower magnetic fields than conventional GaAs-based standards [2–9].

Electrical resistance metrology is based on the integer quantum Hall effect (QHE) in two-dimensional electron gas systems. The resistance plateaus are directly related to an integer fraction of the von Klitzing constant $R_K = h/e^2$ with the Planck constant h and the elementary charge e [10], which are precisely defined values since the revision of the SI in 2019 [11–13]. The cryogenic current comparator (CCC) is a highly sensitive scaling tool used for verification of the quantized resistance [14] and for building a resistance scale at direct current (DC). In practice, the latter includes the calibration of standard resistors with decade nominal values traceable to the quantized Hall resistance (QHR), which can be performed with an uncertainty down to the nΩ/Ω range for selected nominal values [14, 15]. Also, the capacitance unit farad can be derived from QHE measurements using alternating current (AC) [16]. Measurement uncertainties better than 10 nF F^{-1} can be reached using quadrature bridges with two AC-QHR devices linked in multiple-series connection, and by applying the double-shielding technique. The latter was a breakthrough to reduce the impact of inherent capacitive losses leading to curved resistance plateaus depending on the frequency and current [17, 18].

For future quantum impedance standards, it is aimed to use large-area graphene of high quality for the Hall bar fabrication. Epitaxial graphene on silicon carbide (SiC) is well suited to fulfill demands of higher measurement temperatures and lower magnetic fields. However, the inherent high electron density requires a compensation doping procedure to shift the carrier concentration to lower values. Various doping techniques were successfully tested, but they all need a re-tuning procedure before each cool down [19–21]. Recently, DC QHR devices with a stable carrier density were fabricated by applying a post-growth molecular doping technique [22, 23]. However, the compatibility with AC measurements and possible contributions of the dopant molecules to capacitive losses were not yet investigated. Moreover, for reliable use in metrological practice, robustness tests must be carried out concerning different cool-down procedures used in different cryostats, the different handling routines in each laboratory, and last but not least, the impact of transport.

In this study, Hall devices based on epitaxial graphene on SiC from two manufacturers (KRISS and PTB) were investigated on a metrological level in an interlaboratory comparison in three national metrology institutes (CMI, KRISS, and PTB). The carrier density was pre-adjusted by post-growth molecular doping, which made the QHR devices ready for use in the three labs. The stability of the electronic properties, robustness of the devices, and impact of transport were tested by means of high-precision DC and AC QHE measurements.

2. Design, fabrication, and storage of Hall devices

2.1. Graphene growth, functionalization, and main steps in thin-film patterning

At PTB, epitaxial graphene was grown at 1750 °C using the polymer-assisted sublimation growth (PASG) technique [24] on a semi-insulating 6 H-SiC substrate. The device fabrication involved lithographic process steps that minimize the contamination of the graphene with lithographic residues [25, 26]. Instead of individual palladium (Pd) and gold (Au) layers, a modified lithographic process was applied that uses a PdAu alloy (mass ratio of 60% Pd to 40% Au) for the initial graphene protection layer and the later graphene/metal contacts. Before the doping, the Hall device was annealed for 10 min on a hotplate at 90 °C and was subsequently kept in a vacuum chamber under high vacuum for about 16 h at room temperature. After opening the vacuum chamber, the first resist layer (thickness ≈ 100 nm, EL6 copolymer P(MMA (8.5) MAA)) was deposited with a delay of fewer than 5 min. For 2,3,5,6-Tetrafluoro-7,7,8,8-tetracyanoquinodimethane (F4-TCNQ) doping, the 5-layer resist/doping layer system was applied as described in [22, 27].

The final Hall bars provided from PTB (#1 and #2) have a total length of 1600 µm and width of 400 µm, and the distance between two neighboring Hall contact groups is 400 µm. The angle between the direction of the current path along the Hall bar and the direction of the SiC terraces is close to 90°. The electrical contact was realized via a 12-pin transistor outline (TO-8) chip carrier socket. The device design has four instead of six Hall contacts, and the TO-8 chip carrier applied a double shield composed of electrodes above and below the device, which are split into two parts in the center. The device is mounted such that the center pair of Hall contacts is aligned with the gap of the double shield [28]. The double-shield principle enables tuning the capacitive losses by applying voltages to the electrode of the one side of the shield and by shorting the other side of the shield to the low potential current terminal [17, 18].

At KRISS, the growth of epitaxial graphene and the device fabrication were performed in a similar way to the PTB methods. Epitaxial graphene was grown at 1600 °C for 5 min in an argon atmosphere of approximately 100 kPa. To prevent step bunching of the surfaces, we employed the PASG method and a modified graphite susceptor with a small gap for the slow sublimation of silicon atoms. A graphene Hall device was made with electron-beam lithography, oxygen plasma etching for the patterning of the Hall channel, and electrodes. The terrace direction of graphene was determined with an atomic force microscope to align the Hall channel with the terrace direction since the magnetotransport in the quantum Hall regime might be affected by the relative alignment between the terrace and the Hall channel [29]. Pd/Au (20 nm/40 nm) for the metallic contact to the graphene and titanium (Ti)/Au

(3 nm/80 nm) for the contact pads were deposited with an electron-beam evaporator. The width and length of the Hall device are 200 and 880 μm, respectively. The device was annealed at 500 °C for 30 min in a vacuum furnace below about 1 Pa to remove organic residues on graphene from the fabrication processes. The same doping processes [22] with F4-TCNQ were employed in both institutes to reduce the electron carrier density in the graphene channel.

The contact resistances of all devices were inspected by 3-terminal measurements at low temperatures in the quantum Hall regime, and the values of <1 Ω guarantee reliable QHR measurements [14].

2.2. Transportation chamber

To protect the graphene devices during transport against ambient air gas, moisture contamination, and electrostatic charges, a transport chamber for the international delivery was developed. The chamber is made of polycarbonate, and for over-pressure sealing, an O-ring and Allen key bolts are employed. Figure S1 (available online at stacks.iop.org/MST/33/065012/mmedia) in the supplementary material shows details of the chamber. The transport chamber comprises two ports, a pressure gauge, and three metal blocks. Each metal block has a socket in an arrangement of TO-8. The chamber can be over-pressurized with an inert gas during international delivery since it is known that graphene device properties are not influenced by inert gas [22]; this can thus prevent the permeation of water and oxygen molecules from the ambient atmosphere to minimize the degradation of devices. Figure S1 shows the typical pressure drop inside the chamber versus time, which is low enough to conserve the atmosphere during international delivery.

3. Measurement setups

3.1. Precision DC resistance measurements

For DC precision measurements of QHR in graphene Hall devices, the same type of commercial CCC resistance bridge from Magnicon was used for the comparison against 100 Ω reference resistors at CMI, KRISS, and PTB [30–32]. The 100 Ω room temperature resistors were chosen as a reference in our CCC experiment for reasons of comparable thermal noise contributions. At PTB and KRISS, a current of ∼39 μA was applied. At CMI, a current of 23 μA was used. The typical type A uncertainty of the bridge voltage is ⩽0.2 nV/V for a measurement time of about 15 min.

In addition to the type A uncertainty, the combined expanded uncertainties ($k = 2$) of PTB's CCC measurements, as shown along with the results in figures 1 and 2, include type B uncertainties assigned to the involved reference resistors. Table 1 summarizes the uncertainties involved in the R_{xy} measurements with the CCC resistance bridge. The combined uncertainty assigned to the calibration value of the 100 Ω reference resistor is about 1.21 nΩ Ω^{-1}. The subsequent measurement of the 100 Ω reference resistor against the graphene QHR device results in a combined uncertainty of 1.25 nΩ Ω^{-1} ($k = 1$) and a combined expanded uncertainty of 2.5 nΩ Ω^{-1} ($k = 2$), including all known type A and type B uncertainty contributions in the laboratory of the PTB.

Table 2 summarizes the sources and contributions of uncertainties for R_{xx} measurements with the Magnicon CCC resistance bridge. The longitudinal resistance measurements with the CCC are determined from the difference of two individual Hall measurements that includes a type B component attached to the drift of the reference 100 Ω resistor. For a time difference between both measurements of up to 2 h and a maximum drift of 0.5 nV for an applied peak-to-peak voltage of 1 V, a type B uncertainty component of 6 μΩ is added. The resulting combined expanded uncertainty of the longitudinal resistance is about 18 μΩ within the resistance plateau, where R_{xx} is close to zero and has a higher uncertainty outside the plateau due to the increasing instability of the Hall resistance.

3.2. Cryogenic measurement setups

At CMI, the measurement setup is based on a helium bath cryostat with a 14 T magnet and the option to operate at low pressure, leading to an operational temperature range down to 2.3 K. The quantum Hall device (QHD) can be held at this lowered temperature for about 4 h. The cryostat is equipped with a homemade probe VSM12, containing 12 cables for QHD connection and four leads for the Cernox temperature sensor. Coaxial wiring connects the TO-8 socket for the chip carrier to Bayonet Neill-Concelman (BNC) connectors at the room temperature head of the probe. The insulation resistance between adjacent critical pins is higher than 6×10^{13} Ω [33]. The same cryogenic setup was used for DC characterization of the QHD prior to AC measurements. DC properties of the setup were verified during the on-site comparison [32].

KRISS employed two cryostats for interlaboratory comparisons. One is a cold-finger-type cryostat with a base temperature of 2 K for precision measurements of a KRISS device at DC. It comprises a 14 T superconducting magnet and a homemade probe, electrically insulated by a sapphire-spacer from the cold finger. The other system that was used to measure the PTB device at DC and AC is a helium bath cryostat at 4.2 K with a 12 T superconducting magnet for precision measurements. The probe with coaxial cables was home-built based on the design of CMI's probe. To reduce an AC loss stemming from the parasitic capacitance, a double-shield chip carrier [17, 18] was employed. A 12-pin TO-8 socket was connected to BNC connectors at a room temperature break-up box with a cryogenic compatible coaxial cable, having a characteristic impedance of 75 Ω. KRISS used a 12-bit CCC bridge to measure resistances at DC [31].

PTB uses a bath cryostat operating at 4.2 K with a magnet operating at fields up to 12 T. The probe uses the same 12-pin TO-8 socket design and double-shield chip carrier as CMI. The wiring of the probe stick uses coaxial cables with a self-made adapter solution that provides a DC port for the connector of the CCC system.

LNE uses a cryomagnetic setup, which combines a ^{3}He variable-temperature insert and a 20 T superconducting magnet. The homemade cryoprobe applies cables with externally

Table 1. Uncertainty sources and their contributions for R_{xy} measurements with the CCC resistance bridge.

Quantity i	Unc. type	u_i nΩ Ω^{-1}
Typical stability of 100 Ω resistor calibration value ($k = 1$)	B	1.17
Typical type A measurement uncertainty of 100 Ω resistor ($k = 1$)	A	0.30
Syst. errors of CCC for measurement chain R_{xy}—100 Ω—reference QHR ($k = 1$)	B	<0.10
Typical type A measurement uncertainty of R_{xy} ($k = 1$)	A	0.30
Typical combined expanded uncertainty of R_{xy} ($k = 2$)	C	2.50

Table 2. Uncertainty contributions and sources for R_{xx} measurements with the CCC resistance bridge.

Quantity i	u_i $\mu\Omega$
Type B uncertainty due to reference resistor drift ($k = 1$)	6.5
Typical type A measurement uncertainty ($k = 1$)	6.1
Typical combined expanded uncertainty of R_{xx} ($k = 2$)	17.7

Table 3. Contribution of the sources of uncertainties for R_{xy} measurements with CMI's FD bridge at frequency 1233 Hz (in $\mu\Omega$ Ω^{-1}, uncertainty corresponds to $k = 2$).

Quantity i	u_i (R_{xy}) $\times$ 10^6	
Frequency	1233 Hz	5025 Hz
Reference R DC value	0.060	0.060
Reference R AC/DC difference	0.001	0.014
Bridge main balancing	0.040	0.24
Bridge auxiliary balances	0.017	0.035
Bridge reversal stability	0.012	0.023
Bridge imperfections	0.069	0.115
Phase matching	0.006	0.069
Auxiliary capacitor	0.012	0.035
Cable corrections	0.027	0.27
Combined expanded uncertainty	0.11	0.39

Table 4. Uncertainty contribution of R_{xy} measurements with the KRISS' DA bridge at frequency 1541 Hz (in $\mu\Omega$ Ω^{-1}, uncertainty corresponds to $k = 2$).

Quantity i	$u_i(R_{xy})$ $\times$ 10^6
Reference R DC value	0.003
Reference R AC/DC difference	0.004
Bridge main balance	0.008
Bridge imperfections	0.013
Cable corrections	0.085
Repeatability	0.040
Combined expanded uncertainty	0.095

grounded shielding that insulated to the ground by more than 10^{14} Ω for precision electrical measurements. The cryoprobe is terminated by a sample holder hosting two TO-8 sockets with 12 pins each. For DC QHR precision measurements, LNE used a homemade resistance bridge based on a CCC [34].

3.3. Impedance bridges for AC characterization

AC characterizations of the PTB device with the double-shield were performed using coaxial impedance bridges. CMI used a 4-terminal probe (4-TP) digital bridge as described in [35], adapted for triple-series connection of the QHD. The bridge was operated in a fully digital (FD) mode, where the reference arms for the 1:1 ratio resistance measurement were realized by a stable two-channel signal source CMI SWG [36]. To eliminate the reference arm ratio error, measurements with swapped impedance positions against reference signal sources were performed. After the swap of impedances, the bridge was rebalanced with an additional injection generator. With the help of the triple-series connection [37] of QHD in the bridge, fluctuations of voltage drops across wiring resistance between low current ports of the device and the room temperature resistance standard were eliminated. The main contributions of the ratio measurement error came from the reference room temperature resistor, bridge imperfections, cable corrections, and main balancing effects, where the ratio of an injected voltage, bridge voltage, and phase alignment of the null detector is of interest. To minimize residual bridge imbalances, auxiliary and main balances were adjusted to nearly zero. The residual voltage of the main balance was used for numerical correction of the result (usually at the level of 10 nΩ Ω^{-1}). The influence of the stability of the reference voltage source SWG on the ratio measurement accuracy was at the level of 10 nΩ Ω^{-1} for a few hours of ratio measurements. Due to low cable resistances of the QHD probe (lower than 0.8 Ω for inner wire and outer screen together) and the application of active current equalizers in the wiring around QHD, the effect of unequal currents in the cables was negligible. The uncertainty of R_{xy} measurement is 0.11 $\mu\Omega$ Ω^{-1} for frequency 1233 Hz (sources given in table 3). For R_{xy} measurements at 5025 Hz and the characterization of the plateau shape near the quantized value $R_K/2$, the uncertainty increases to 0.39 $\mu\Omega$ Ω^{-1}, mainly due to cable corrections.

As a reference impedance with known frequency dependence, an octofilar type resistor [38] with a calculable frequency dependence of the resistance and time constant was used. The R_{xy} correction on the level of 15 nΩ Ω^{-1} at 1 kHz with an uncertainty on the level of a few nΩ Ω^{-1} for the AC/DC difference of the resistance standard was taken into account.

KRISS has performed AC measurements with the same PTB device with the 4-TP digital bridge described in [35] but in a digitally assisted (DA) mode. As a reference impedance, a quadrifilar type resistor close to the nominal value of $R_K/2$ with a calculable frequency dependence was used. At the frequency of 1541 Hz, the calculable frequency dependence was about 73 nΩ Ω^{-1} with an uncertainty on the 10^{-9} level. The QHD was connected to the bridge via a triple-series

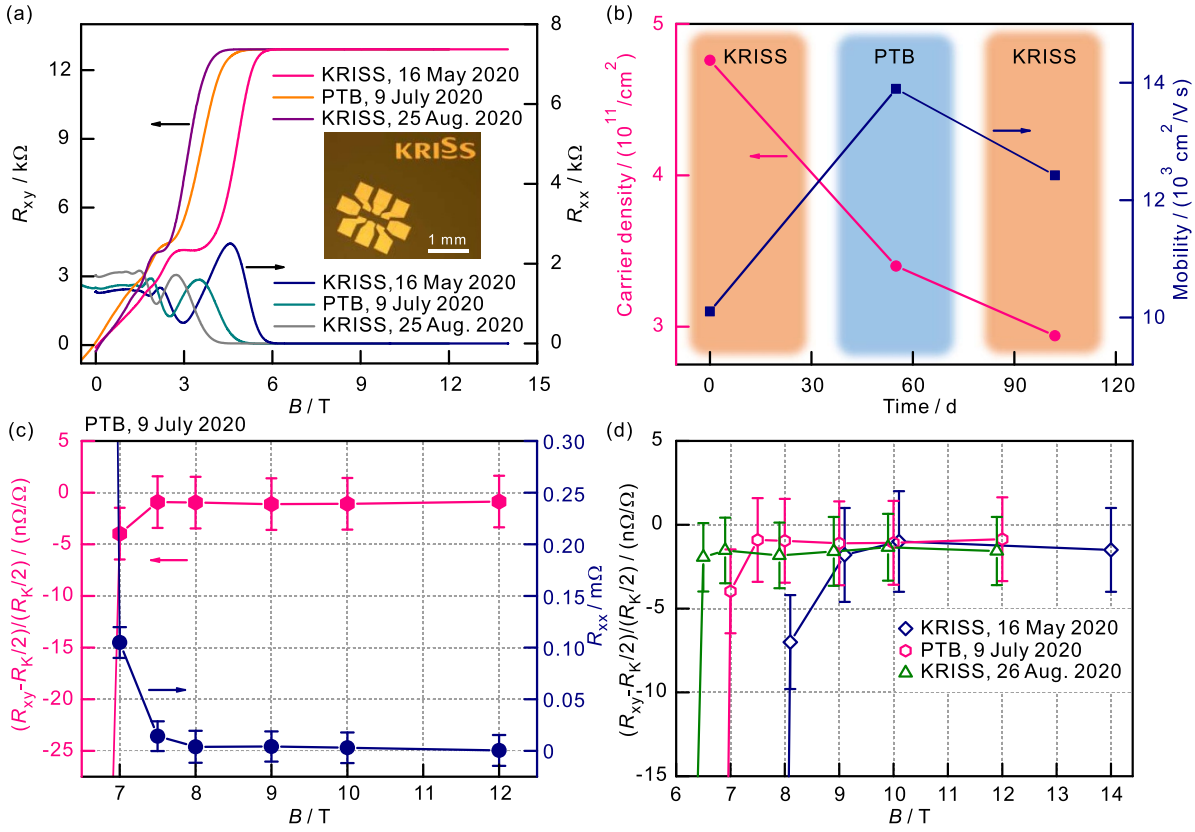

Figure 1. Round-trip DC characterization of the KRISS device from KRISS to PTB. (a) Magnetoresistance measurements at 4.2 K. Inset shows an optical microscope image of the measured device. (b) Carrier density and mobility versus time. (c) Relative deviation of quantum Hall resistance at filling factor 2 from the nominal value of $R_K/2$ and the longitudinal resistance, depicted by the red hexagon and blue dot, respectively, as a function of the magnetic field. (d) Relative deviation in the interlaboratory comparison. For better visibility, several data points were slightly shifted in the magnetic field.

connection scheme. The cable resistance of the QHD probe was approximately 1.5 Ω at 4 K, and the active current equalizers were applied to equalize the currents in the cables effectively. The ratio error of the main ratio transformer was eliminated by means of swapping the impedance positions. The expanded measurement uncertainty of R_{xy} measurement is about 0.1 μΩ Ω^{-1} for the frequency 1541 Hz (sources given in table 4). Main contributions come from the cable corrections and the type A repeatability, which includes the stabilities of the reference impedance and auxiliary balances and the voltage generation repeatability for the main balance injection. Under the circumstance of the triple-series connection of the QHD and the 4-TP connection for the reference impedance, the cable correction terms do not cancel out even for the 1:1 comparison [37].

4. Experimental results

4.1. Stability of graphene devices through international delivery

Figure 1 shows the DC resistance quantization and stability of the transport properties during an international exchange of the KRISS device. The interlaboratory comparison between KRISS and PTB was performed through standard air freight delivery with the described transport chamber. Figure 1(a) shows magnetoresistance measurements at 4.2 K. The hole-type charge-carrier density and mobility values in figure 1(b) are extracted from the magnetoresistance in the classical Hall regime in figure 1(a). The hole density decreases during the transport from KRISS to PTB as well as during the shipping back to KRISS over the course of nearly 3.5 months, resulting in a total change of about $\Delta p = 2 \times 10^{11}\,\mathrm{cm}^{-2}$. The red hexagonal data points in figure 1(c) shows the relative deviation from the nominal Hall resistance value of $R_K/2$ versus the magnetic field measured at PTB and a beginning of the well-quantized region starting at $B = 7.5$ T. The corresponding longitudinal resistance is represented by the blue dots with values below 50 μΩ for $B \geqslant 7.5$ T. The data points in figure 1(d) summarize all relative deviations measured in the bilateral comparison between KRISS and PTB of the KRISS device. The shift to lower charge-carrier densities resulted in a lowering of the beginning of the well-quantized region from $B = 9.0$ T to around $B = 6.5$ T and thus helped to improve the quantization behavior. Despite the moderate changes in the hole density, the device was well quantized over a wide magnetic field range within a few nΩ Ω^{-1}. We note that there is still a deviation of Hall quantization from $R_K/2$ as shown in figures 1(c) and (d), corresponding to the combined expanded uncertainty, although this deviation is smaller than the error

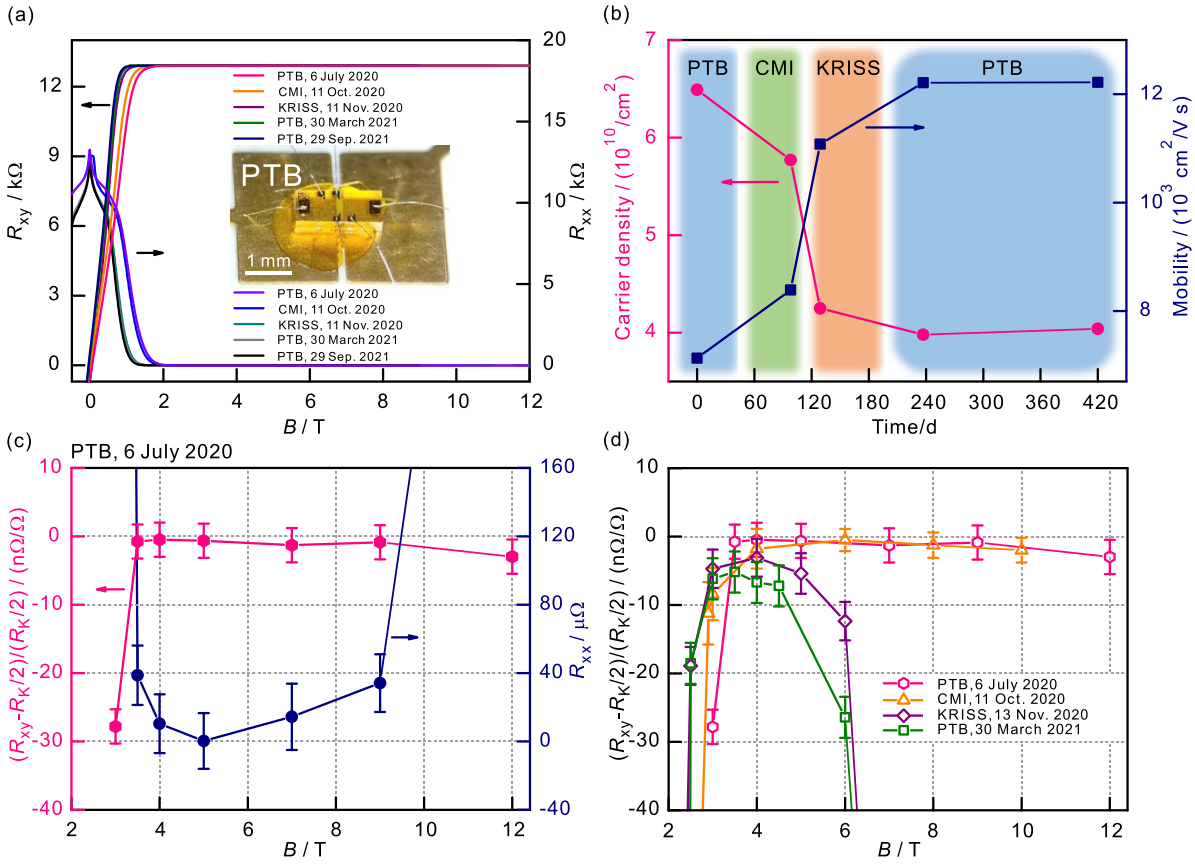

Figure 2. Round-robin DC characterization of the PTB device #1 in the double-shield packaging among PTB, CMI, and KRISS. (a) Magnetoresistance measurements at 4.2 K. The inset shows a photograph of the measured device without a top shield. (b) Carrier density and mobility versus time. (c) Relative deviation of the quantum Hall plateau at filling factor 2 from the nominal value of $R_K/2$ and longitudinal resistance, depicted by the red hexagon and blue dot, respectively, as a function of the magnetic field. This initial data set was measured by PTB. (d) The relative deviations were measured in the sequence of PTB, CMI, KRISS, and again PTB.

bar. The observed deviation might be attributed to graphene quality itself or disorders arising from the device-fabrication procedure. However, we still cannot exclude a possible current leakage through either the molecular dopant layer [22] or the semi-insulating SiC substrate. Also, this deviation might be attributed to an insulation difference [22] between two different employed cryomagnets for graphene and GaAs devices at each institute, requiring a further investigation.

Figure 2 represents the DC resistance quantization behavior and the stability of the electronic transport properties during the international exchange of the PTB device #1. The inset of figure 2(a) shows a photograph of the device mounted on the TO-8 chip carrier with a double shield specifically designed for AC measurements. Note that the charge carrier type is also hole type, and that its initial hole density of approximately $p = 6.5 \times 10^{10}\,\mathrm{cm}^{-2}$ is almost 1 order of magnitude lower than that of the KRISS device. Consequently, the Hall plateau also starts at significantly lower magnetic field values. Figure 2(a) summarizes magnetoresistances sequentially measured at PTB, CMI, KRISS, and again PTB. Figure 2(b) shows the changes in the carrier density and mobility values between the measurements of the three institutes during the storage and transport of the device. The total change over the course of about 8 months was about $\Delta p = 2.5 \times 10^{10}\,\mathrm{cm}^{-2}$. Figure 2(c) depicts the initial relative deviation from $R_K/2$ as a function of the magnetic field and verifies that the device was well quantized between $B = 3.5$ T and $B = 9$ T when measured at PTB despite the low charge-carrier density. Within this well-quantized region, the longitudinal resistance dropped to values $\leqslant 50\ \mu\Omega$. Figure 2(d) summarizes precision measurements of the QHR at DC in the sequence of PTB, CMI, KRISS, and PTB. We observed that the magnetic field range in which the device showed good quantization behavior was narrowed over time, accompanied by changes in the charge-carrier density.

Literature values suggest that the optimal electron charge-carrier density of devices for quantum resistance metrology is usually between $3.0 \times 10^{11}\,\mathrm{cm}^{-2}$ and $1.0 \times 10^{11}\,\mathrm{cm}^{-2}$ if resistance quantization is aimed to start below $B = 7.5$ T or even below $B = 5$ T [8, 9, 39]. While the device in figure 2 was still very well quantized at its initial charge-carrier density of $6.5 \times 10^{10}\,\mathrm{cm}^{-2}$, the magnetoresistance measurements show a reduction of the hole density accompanied by a narrowing of the well-quantized region. A narrowing of the QHR plateau and increased longitudinal resistance at carrier densities below $1.0 \times 10^{11}\,\mathrm{cm}^{-2}$ can be qualitatively understood with physics of nonuniform transport properties near the charge neutrality. This implies that the carrier density entered from a homogenous hole-conduction regime into an

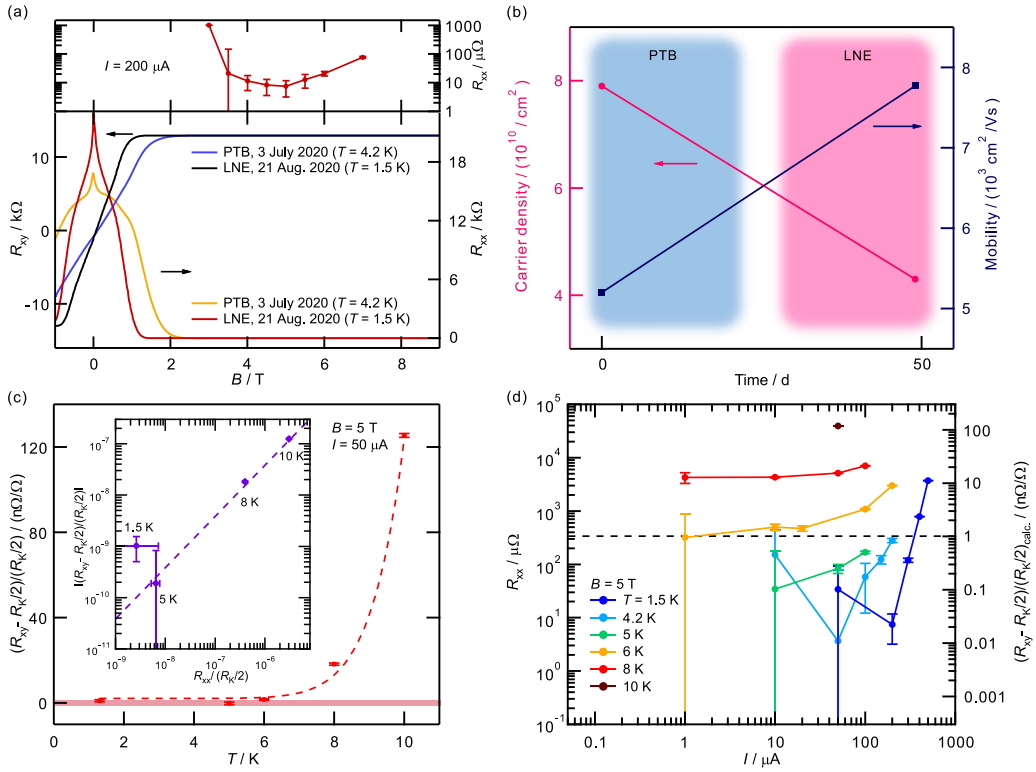

Figure 3. Stability of the PTB device (#2) at high temperature and high DC current. (a) Bottom panel: Hall resistance R_{xy} and longitudinal resistance per square R_{xx} as a function of the magnetic field B, measured at PTB ($T = 4.2$ K) and at LNE ($T = 1.5$ K). It is the same design as PTB #1. Top panel: Precision measurements of R_{xx} as a function of the magnetic field at a measurement current $I = 200$ μA and temperature $T = 1.5$ K. (b) Low-temperature carrier density and mobility versus time were successively measured at PTB and LNE. (c) Relative deviation of the quantum Hall resistance at filling factor 2 from the nominal value of $R_K/2$, as a function of temperature. The dashed line is a guide for the eyes. The inset shows theses deviations plotted as a function of the corresponding R_{xx} values relative to $R_K/2$. (d) Longitudinal resistance as a function of the measurement current at different temperatures. The right axis shows the corresponding relative deviation of the quantum Hall resistance at filling factor 2, calculated from the longitudinal resistance values and the coupling factor s determined from (c).

inhomogeneous electron–hole puddle [40] regime near charge neutrality. According to previous studies, the random potential disorder of electron–hole puddles can cause a broadening and overlapping of extended states of the zeroth and first Landau levels, leading to a deviation from the nominal resistance value of the filling factor 2 plateau [41, 42].

4.2. Stability of a graphene device at high temperature and high DC current

In order to fully probe the regime of operation of the QHDs, namely not only in the magnetic field range but also in temperature T and measurement DC current I, another device made at PTB (#2) traveled from PTB to LNE using the previously described transport chamber. Prior to its delivery to LNE, the device was characterized at PTB. Figure 3(a) (lower panel) shows the magnetoresistance measured both at PTB ($T = 4.2$ K) and at LNE ($T = 1.5$ K), from which we extracted the charge-carrier density and mobility (figure 3(b)). The hole-type carrier density decreased after transportation from PTB to LNE, with a change of about $\Delta p = 4 \times 10^{10}\,\mathrm{cm}^{-2}$ over 49 d.

Figure 3(a) (upper panel) shows precision measurements of the longitudinal resistance per square R_{xx} in the $i = 2$ plateau at $T = 1.5$ K, as a function of the magnetic field B and at a high DC current $I = 200$ μA. The minimum of dissipation is clearly visible at $B = 5$ T. This magnetic field is much higher than the value at which the $i = 2$ plateau is expected, knowing the value of the charge-carrier density $\left(B_{i=2} = \frac{nh}{2e} = 0.89\ T\right)$, which thus suggests a transfer of charge, as reported in the literature for epitaxial graphene grown on SiC in the quantum Hall regime [43]. Note that the same optimum magnetic field was observable in figure 2(c) for the other PTB device. This tends to indicate a high uniformity of the quantum Hall transport properties for different devices processed from graphene coming from the same growth batch. In the following, we will focus on precision measurements of R_{xx} and R_{xy} performed at this particular magnetic field, as a function of both T and I, in order to test the robustness of the Hall quantization.

As stated in the technical guidelines for reliable DC QHR measurements [14], varying the temperature while keeping the measurement current constant is an important characterization technique of QHDs. This comes from the fact that a finite temperature—and also a finite current—is predicted to induce a deviation of the Hall resistance from the perfect quantization, which has to be kept lower than the measurement uncertainty for the application of the device as a resistance

standard. Figure 3(c) thus shows the relative deviation of the Hall resistance at filling factor 2 from its nominal value, $R_K/2$, plotted as a function of temperature. The regime where R_{xy} is accurately quantized, with no significant deviation within the relative combined standard uncertainty of the measurement ($k = 1$; equal to 1 nΩ/Ω) is emphasized by the red area. No deviation from the quantized value is observed up to $T = 6$ K within a 2-sigma uncertainty. Moreover, we have plotted these measured values of the deviation of the Hall resistance from $R_K/2$ as a function of the corresponding values of the longitudinal resistance per square, relative to $R_K/2$ (inset of figure 3(c)). The dashed line has a slope of unity and therefore indicates a linear fitting in the log—log scale and thus reflects the relation $\Delta R_{xy}/(R_K/2) = sR_{xx}/(R_K/2)$, as usually observed in QHDs by metrologists [44]. The extracted value of the coupling factor $s = 0.038$, below 0.1, is consistent with former determinations of s for graphene devices at PTB [45]. In other words, this value of s means that the Hall resistance is expected to remain accurately quantized to within 1 nΩ Ω^{-1} in relative value for a longitudinal resistance per square smaller than $R_{xx} \leqslant 337\mu\Omega$.

The operation of QHDs at high measurement current is essential to maximize the signal-to-noise ratio. Figure 3(d) shows the evolution of the measured longitudinal resistance per square (left axis) with DC at different temperatures. The right axis represents the calculated values of the corresponding relative deviation of R_{xy} from $R_K/2$ by taking into account the coupling factor s previously determined. The horizontal dashed line marks the threshold level of dissipation ($R_{xx} \leqslant 337\mu\Omega$) above which relative deviations of R_{xy} are expected to exceed 1 nΩ Ω^{-1}. At high temperature ($T > 6$ K), a significant longitudinal resistance is measured even in the limit of small measurement current, which therefore prevents accurate quantization of the Hall resistance. At low temperature ($T = 1.5$ K), accurate quantization of the Hall resistance is therefore expected for a measurement current below the value I_{max} of about 350 μA, while at moderate temperature ($T = 4.2$ K), $I_{max} \simeq 200\,\mu A$.

4.3. AC behavior of quantized Hall resistance plateau

Figure 4 shows Hall resistance measurements of the PTB device #1 in the double-shield geometry at AC. The measurements were performed sequentially at CMI and KRISS as described in the experimental method at a current of 23 μA. Figure 4(a) shows the relative differences of R_{xy} between 2 and 8 T, measured at frequencies of 1233 and 5025 Hz at CMI. When a linear frequency dependence is assumed, a negative frequency dependence of about −0.15 μΩ/Ω/kHz, for instance, at the magnetic field of 4 T was observed. The time constant of the device was measured and found to be (−1.2 ± 2.3) ns. The main contribution to the uncertainty of the time constant was the reference room temperature resistor. KRISS measured R_{xy} at the frequency of 1541 Hz. The relative difference between 2 and 9 T is shown in figure 4(b). While the R_{xy} in figure 4(a) was measured continuously, that of figure 4(b) was measured discretely at each magnetic field.

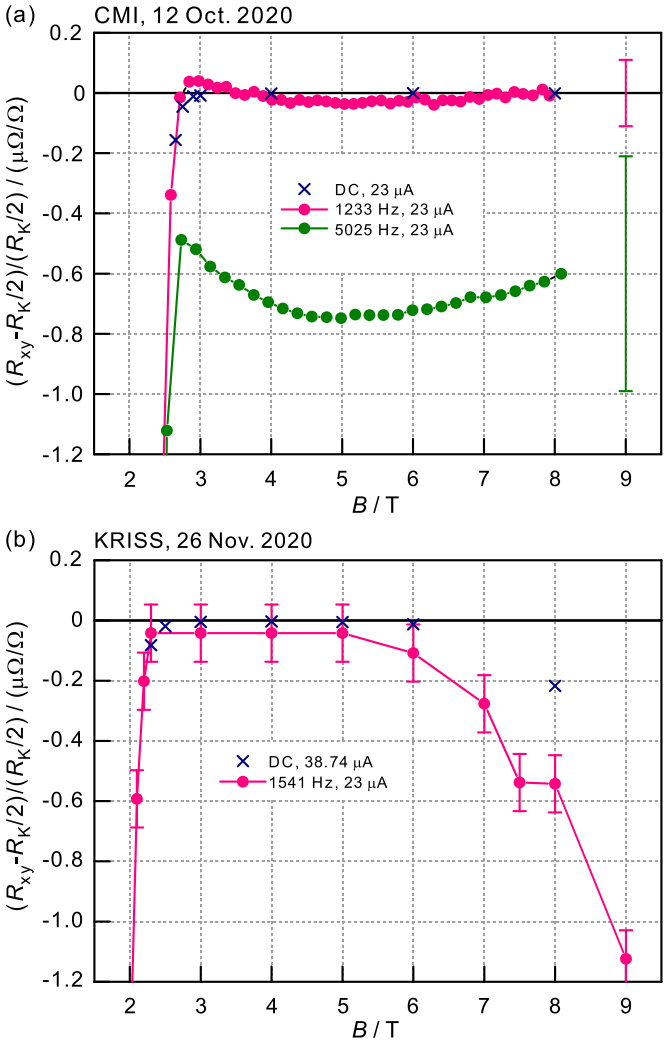

Figure 4. Relative difference of the quantum Hall plateau at filling factor 2 from the nominal value of $R_K/2$ as a function of the magnetic field at DC and AC in the PTB device at 4.2 K. (a) Relative differences measured at CMI. DC results are replotted with × symbol using the CMI data set in figure 2(d). Uncertainty bars for 1233 and 5025 Hz are depicted by red and green bars, respectively. (b) Relative differences measured at KRISS. DC results are replotted with × symbol using the KRISS data set in figure 2(d).

A negative frequency dependence was confirmed from additional measurements performed up to frequency 4025 Hz. The measurement of R_{xy} performed 45 d later at KRISS shows different curvatures of the plateau for both DC and AC regimes. This is assumed to be related to the reduction of the carrier density with time.

The negative R_{xy} frequency dependence agrees with most of the previously published results for graphene devices, e.g. [46]. It is expected that a linear frequency dependence can be caused by lossy currents through dissipative parasitic capacitances between the graphene channel of the QHD and its surroundings [18]. The potential of the high shield between high-current contact and defining Hall-potential terminals (HPTs) was maintained at zero in CMI and KRISS. In principle, the dissipative capacitance $C_{Hpe1\text{-}HS}$ between the high potential

edge of the QHD (the part after HPTs from the point of view of current flow) and the high shield introduces an increment of R_{xy} against the frequency. In contrast, the capacitance $C_{Hpe2\text{-}LS}$ between the high potential edge (part before HPTs) and the low shield introduces a decrement of R_{xy} against the frequency. The position of the Hall probe in the investigated device was slightly shifted away from the center of the chip carrier towards the low shield. Hence, the capacitance $C_{Hpe2\text{-}LS}$ was higher than $C_{Hpe1\text{-}HS}$, resulting in a negative frequency dependence. Since positive slopes were observed in the cases of large devices or devices without the double shields or modified contact geometry [45], we can assume that a negligible frequency dependence may be achieved with further optimization of the device geometry.

In the AC regime, we also expect a frequency-dependent deviation from the nominal QHR value that additionally depends on the charge-carrier density. This is because the intrinsic quantum capacitance is defined by the product of the squared elementary charge and the density of states (DOS) at the chemical potential [47]. This intrinsic capacitance likely contributes to the deviation from the nominal QHR value at AC and is proportional to the frequency [48, 49]. This qualitative argument is consistent with our observations in this study and previous works [45, 46, 50], but the quantitative effects of the charge carrier density will require further systematic experimental investigations.

5. Summary

This interlaboratory investigation demonstrates that precision QHR measurements in graphene can be performed at a level of 1 nΩ Ω^{-1} at DC, and at a level of about 0.1 μΩ Ω^{-1} at AC despite overseas transport. The devices were fabricated in different cleanroom facilities using distinct lithographic processes but applied the same F4-TCNQ doping technique, resulting in p-type conductivity in both facilities. The sharp drop of the longitudinal resistance to values below 50 μΩ and the early onset of the well-quantized resistance plateau at relatively low magnetic field demonstrate the highly uniform transport properties. While the KRISS device showed good resistance quantization behavior down to B-field values of $B = 6.5$ T at a carrier density at the level of $p \approx 3 \times 10^{11}$ cm^{-2}, the PTB device started to be well quantized at $B = 3.5$ T and $p \approx 6 \times 10^{10}$ cm^{-2}. The observed shift in the charge-carrier density in the KRISS device of $\Delta p \approx 2 \times 10^{11}$ cm^{-2}, of the PTB device 1 of $\Delta p \approx 2.5 \times 10^{10}$ cm^{-2}, and of the PTB device 2 of $\Delta p = 4 \times 10^{10}$ cm^{-2} were observed over time, especially during the long-distance shipping in inert gas containers. Such changes can be critical, especially in the case of low initial charge-carrier densities since the device can quickly shift into the electron–hole puddle regime, as was observed for PTB's device 1 after the transport from CMI to KRISS. Moderate initial carrier densities between $p \approx 1 \times 10^{11}$ cm^{-2} and $p \approx 2 \times 10^{11}$ cm^{-2} using F4-TCNQ doping are expected to be better suited to increasing the device stability, as they would provide a higher tolerance against moderate changes while maintaining accurate resistance quantization at magnetic field values around $B \sim 5.0$ T. We also investigated the robustness of the Hall quantization with respect to temperature and applied current. For the second PTB device, we found that at $T = 4.2$ K and $B = 5$ T, a current of up to 200 μA can be applied while maintaining resistance quantization with a precision on the level of 1 nΩ Ω^{-1}. In summary, the applied device fabrication and especially the F4-TCNQ doping technique enable highly uniform transport properties and advanced stability, which are both requirements for next-generation AC and DC electrical QHR standards. To our knowledge, this is the first reported in-depth metrological study of graphene QHR devices performed with precision DC and AC resistance bridges in the p-type regime.

Data availability statement

The data that support the findings of this study are available upon reasonable request from the authors.

Acknowledgments

This work was supported by the Joint Research Project 18SIB07 GIQS—*Graphene Impedance Quantum Standard*. This project has received funding from the EMPIR programme co-financed by the Participating States and from the European Union's Horizon 2020 research and innovation programme. In Korea, this collaborative work was supported by the National Research Foundation of Korea (Grant No. NRF-2019K1A3A1A78077479). The visit at KRISS of N T M Tran was funded by the joint PhD programme of Politecnico di Torino and INRIM.

Disclaimer

Commercial equipment, instruments, and materials are identified in this paper in order to specify the experimental procedure adequately. Such identification is not intended to imply recommendation or endorsement by the contributing institutes and authors, nor is it intended to imply that the materials or equipment identified are necessarily the best available for the purpose.

ORCID iDs

Dong-Hun Chae https://orcid.org/0000-0001-6394-9182
Mattias Kruskopf https://orcid.org/0000-0003-2846-3157
Jan Kucera https://orcid.org/0000-0003-3209-8594
Dan Bee Kim https://orcid.org/0000-0002-5992-0990
Klaus Pierz https://orcid.org/0000-0001-6400-1799
François Couëdo https://orcid.org/0000-0003-0084-7271

References

[1] Novoselov K S, Jiang Z, Zhang Y, Morozov S V, Stormer H L, Zeitler U, Maan J C, Boebinger G S, Kim P and Geim A K 2007 Room-temperature quantum Hall effect in graphene *Science* **315** 1379

[2] Giesbers A J M, Rietveld G, Houtzager E, Zeitler U, Yang R, Novoselov K S, Geim A K and Maan J C 2008 Quantum resistance metrology in graphene *Appl. Phys. Lett.* **93** 2–5

[3] Tzalenchuk A, Lara-Avila S, Kalaboukhov A, Paolillo S, Syväjärvi M, Yakimova R, Kazakova O, Janssen T J B M, Fal'ko V and Kubatkin S 2010 Towards a quantum resistance standard based on epitaxial graphene *Nat. Nanotechnol.* **5** 186–9

[4] Janssen T J B M, Fletcher N E, Goebel R, Williams J M, Tzalenchuk A, Yakimova R, Kubatkin S, Lara-Avila S and Falko V I 2011 Graphene, universality of the quantum Hall effect and redefinition of the SI system *New J. Phys.* **13** 093026

[5] Woszczyna M, Friedemann M, Götz M, Pesel E, Pierz K, Weimann T and Ahlers F J 2012 Precision quantization of Hall resistance in transferred graphene *Appl. Phys. Lett.* **100** 16–19

[6] Janssen T J B M, Tzalenchuk A, Lara-Avila S, Kubatkin S and Fal'ko V I 2013 Quantum resistance metrology using graphene *Rep. Prog. Phys.* **76** 104501

[7] Satrapinski A, Novikov S and Lebedeva N 2013 Precision quantum Hall resistance measurement on epitaxial graphene device in low magnetic field *Appl. Phys. Lett.* **103** 1–5

[8] Lafont F *et al* 2015 Quantum Hall resistance standards from graphene grown by chemical vapour deposition on silicon carbide *Nat. Commun.* **6** 6806

[9] Ribeiro-Palau R *et al* 2015 Quantum Hall resistance standard in graphene devices under relaxed experimental conditions *Nat. Nanotechnol.* **10** 965–71

[10] Klitzing K V, Dorda G and Pepper M 1980 New method for high-accuracy determination of the fine-structure constant based on quantized Hall resistance *Phys. Rev. Lett.* **45** 494–7

[11] Bureau International des Poids et Mesures (BIPM) 2018 *Proc. 26th Meeting of the General Conf. on Weights and Measures (November 2018)* (Imprimerie Agate)

[12] Göbel E and Siegner U 2019 *The New International System of Units (SI)* (New York: Wiley)

[13] Rigosi A F and Elmquist R E 2019 The quantum Hall effect in the era of the new SI *Semicond. Sci. Technol.* **34** 093004

[14] Delahaye F and Jeckelmann B 2003 Revised technical guidelines for reliable DC measurements of the quantized Hall resistance *Metrologia* **40** 217–23

[15] Jeckelmann B and Jeanneret B 2001 The quantum Hall effect as an electrical resistance standard *Rep. Prog. Phys.* **64** 1603–55

[16] Melcher J, Warnecke P and Hanke R 1993 Comparison of precision AC and DC measurements with the quantized Hall resistance *IEEE Trans. Instrum. Meas.* **42** 292–4

[17] Kibble B P and Schurr J 2008 A novel double-shielding technique for AC quantum Hall measurement *Metrologia* **45** L25–L27

[18] Schurr J, Kučera J, Pierz K and Kibble B P 2011 The quantum Hall impedance standard *Metrologia* **48** 47–57

[19] Lara-Avila S, Moth-Poulsen K, Yakimova R, Bjørnholm T, Fal'ko V, Tzalenchuk A and Kubatkin S 2011 Non-volatile photochemical gating of an epitaxial graphene/polymer heterostructure *Adv. Mater.* **23** 878–82

[20] Lartsev A, Yager T, Bergsten T, Tzalenchuk A, Janssen T J B M, Yakimova R, Lara-Avila S and Kubatkin S 2014 Tuning carrier density across Dirac point in epitaxial graphene on SiC by corona discharge *Appl. Phys. Lett.* **105** 10–14

[21] Rigosi A F *et al* 2019 Gateless and reversible carrier density tunability in epitaxial graphene devices functionalized with chromium tricarbonyl *Carbon* **142** 468–74

[22] He H *et al* 2019 Polymer-encapsulated molecular doped epigraphene for quantum resistance metrology *Metrologia* **56** 045004

[23] He H *et al* 2018 Uniform doping of graphene close to the Dirac point by polymer-assisted assembly of molecular dopants *Nat. Commun.* **9** 3–9

[24] Kruskopf M *et al* 2016 Comeback of epitaxial graphene for electronics: large-area growth of bilayer-free graphene on SiC *2D Mater.* **3** 1–9

[25] Yang Y, Huang L I, Fukuyama Y, Liu F H, Real M A, Barbara P, Te Liang C, Newell D B and Elmquist R E 2015 Low carrier density epitaxial graphene devices on SiC *Small* **11** 90–95

[26] Yang Y *et al* 2017 Epitaxial graphene homogeneity and quantum Hall effect in millimeter-scale devices *Carbon* **115** 229–36

[27] He H 2020 *Molecular Doping of Epitaxial Graphene—For Device Applications* (Göteborg: Chalmers University of Technology)

[28] Schurr J, Kibble B P, Hein G and Pierz K 2009 Controlling losses with gates and shields to perfect a quantum Hall impedance standard *IEEE Trans. Instrum. Meas.* **58** 973–9

[29] Schumann T, Friedland K-J, Oliveira M H, Tahraoui A, Lopes J M J and Riechert H 2012 Anisotropic quantum Hall effect in epitaxial graphene on stepped SiC surfaces *Phys. Rev.* B **85** 235402

[30] Gotz M, Drung D, Pesel E, Barthelmess H-J, Hinnrichs C, Assmann C, Peters M, Scherer H, Schumacher B and Schurig T 2009 Improved cryogenic current comparator setup with digital current sources *IEEE Trans. Instrum. Meas.* **58** 1176–82

[31] Gournay P, Rolland B, Chae D-H and Kim W-S 2020 On-site comparison of quantum hall effect resistance standards of the KRISS and the BIPM: ongoing key comparison BIPM.EM-K12 *Metrologia* **57** 01010

[32] Gournay P, Rolland B, Kučera J and Vojáčková L 2017 On-site comparison of quantum Hall effect resistance standards of the CMI and the BIPM: ongoing key comparison BIPM.EM-K12 *Metrologia* **54** 01014

[33] Kucera J, Svoboda P and Pierz K 2019 AC and DC quantum Hall measurements in gaas-based devices at temperatures up to 4.2 K *IEEE Trans. Instrum. Meas.* **68** 2106–12

[34] Poirier W, Leprat D and Schopfer F 2021 A resistance bridge based on a cryogenic current comparator achieving sub-10^{-9} measurement uncertainties *IEEE Trans. Instrum. Meas.* **70** 1000314

[35] Kucera J and Kovac J 2018 A reconfigurable four terminal-pair digitally assisted and fully digital impedance ratio bridge *IEEE Trans. Instrum. Meas.* **67** 1199–206

[36] Kucera J, Kovac J, Palafox L, Behr R and Vojackova L 2020 Characterization of a precision modular sinewave generator *Meas. Sci. Technol.* **31** 064002

[37] Awan S, Kibble B and Schurr J 2011 *Coaxial Electrical Circuits for Interference-Free Measurements* (London: Institution of Engineering and Technology)

[38] Bohácek J and Wood B M 2001 Octofilar resistors with calculable frequency dependence *Metrologia* **38** 241–7

[39] Kruskopf M and Elmquist R E 2018 Epitaxial graphene for quantum resistance metrology *Metrologia* **55** R27–R36

[40] Martin J, Akerman N, Ulbricht G, Lohmann T, Smet J H, von Klitzing K and Yacoby A 2008 Observation of electron-hole puddles in graphene using a scanning single-electron transistor *Nat. Phys.* **4** 144–8

[41] Takase K, Hibino H and Muraki K 2015 Probing the extended-state width of disorder-broadened Landau levels in epitaxial graphene *Phys. Rev.* B **92** 125407

[42] Lara-Avila S, Tzalenchuk A, Kubatkin S, Yakimova R, Janssen T J B M, Cedergren K, Bergsten T and Fal'ko V 2011 Disordered Fermi liquid in epitaxial graphene from

quantum transport measurements *Phys. Rev. Lett.* **107** 166602
[43] Janssen T J B M, Tzalenchuk A, Yakimova R, Kubatkin S, Lara-Avila S, Kopylov S V and Fal'Ko V I 2011 Anomalously strong pinning of the filling factor $\nu=2$ in epitaxial graphene *Phys. Rev.* B **83** 3–6
[44] Cage M E, Field B F, Dziuba R F, Girvin S M, Gossard A C and Tsui D C 1984 Temperature dependence of the quantum Hall resistance *Phys. Rev.* B **30** 2286–9
[45] Kruskopf M *et al* 2021 Graphene quantum Hall effect devices for AC and DC electrical metrology *IEEE Trans. Electron Devices* **68** 3672–7
[46] Lüönd F, Kalmbach C-C, Overney F, Schurr J, Jeanneret B, Müller A, Kruskopf M, Pierz K and Ahlers F 2017 AC quantum Hall effect in epitaxial graphene *IEEE Trans. Instrum. Meas.* **66** 1459–66
[47] Ponomarenko L A, Yang R, Gorbachev R V, Blake P, Mayorov A S, Novoselov K S, Katsnelson M I and Geim A K 2010 Density of states and zero Landau level probed through capacitance of graphene *Phys. Rev. Lett.* **105** 136801
[48] Christen T and Büttiker M 1996 Low-frequency admittance of quantized Hall conductors *Phys. Rev.* B **53** 2064–72
[49] Jeanneret B and Overney F 2007 Phenomenological model for frequency-related dissipation in the quantized Hall resistance *IEEE Trans. Instrum. Meas.* **56** 431–4
[50] Schurr J, Kalmbach C-C, Ahlers F J, Hohls F, Kruskopf M, Müller A, Pierz K, Bergsten T and Haug R J 2017 Magnetocapacitance and dissipation factor of epitaxial graphene-based quantum Hall effect devices *Phys. Rev.* B **96** 155443